



A Cost-Effective and High-Performance Core-Shell-Nanorod-Based ZnO/ α -Fe₂O₃//ZnO/C Asymmetric Supercapacitor

Debashish Sarkar,^{a,*} Shyamashis Das,^a Sharada G,^a Banabir Pal,^a Håkan Rensmo,^b Ashok Shukla,^{a,**} and D. D. Sarma^{a,b,z}

^aSolid state and Structural Chemistry Unit, Indian Institute of Science, Bengaluru 560012, India

^bDepartment of Physics and Astronomy, Uppsala University, SE 75120 Uppsala, Sweden

A novel core-shell design for nano-structured electrode materials is introduced for realizing cost-effective and high-performance supercapacitors. In the proposed core-shell design, thin shell-layers of highly pseudo-capacitive materials provide the platform for surface or near-surface-based faradaic and non-faradaic reactions together with shortened ion-diffusion path facilitating fast-ion intercalation and deintercalation processes. The highly-conducting core serves as highway for fast electron transfer toward current collectors, improving both energy and power performance characteristics of the core-shell structure in relation to pristine component materials. Furthermore, use of carbon (C)-based materials as a shell layer in either electrode not only enhances capacitive performance through double-layer formation but also provides enough mechanical strength to sustain volume changes in the core material during long-cycling of the supercapacitor improving its cycle life. In order to enhance electrochemical performance in terms of specific capacitance and rate capability via core-shell architecture and nano-structuring, an asymmetric supercapacitor (ASC) is assembled using ZnO/ α -Fe₂O₃ and ZnO/C core-shell nanorods as respective negative and positive electrodes. The ASC exhibits a specific capacitance of \sim 115 F/g at a scan rate of 10 mV/s in a potential window as large as 1.8 V with a response time as short as \sim 39 ms and retains more than 80% of its initial capacitance after 4000 cycles. Interestingly, the ASC can deliver an energy density of \sim 41 Wh/kg and a power density of \sim 7 kW/kg that are significantly higher than those reported hitherto for iron-oxide-based ASCs.

© The Author(s) 2017. Published by ECS. This is an open access article distributed under the terms of the Creative Commons Attribution 4.0 License (CC BY, <http://creativecommons.org/licenses/by/4.0/>), which permits unrestricted reuse of the work in any medium, provided the original work is properly cited. [DOI: [10.1149/2.0351706jes](https://doi.org/10.1149/2.0351706jes)] All rights reserved.



Manuscript submitted December 20, 2016; revised manuscript received January 30, 2017. Published March 15, 2017. This was Paper 65 presented at the Honolulu, Hawaii, Meeting of the Society, October 2–7, 2016.

Global concern over ever increasing greenhouse gas emissions owing to exorbitant anthropogenic usage of fossil fuels is forcing governments across the globe to swing toward renewable energy sources. Since renewable sources of energy, like sun and wind, are intermittent in nature, it becomes mandatory to store the energy from these sources that could be retrieved on demand. Accordingly, the missing link in successful exploitation of renewable energy is its storage.¹ Electrochemical storage of energy in storage-batteries is attractive but supercapacitors are gaining attention due to their compelling power densities as well as fast charge and discharge traits.^{2,3} It is noteworthy that a battery is an energy device while a supercapacitor is a power device. If we require high power from a battery, we will generally extract less total energy than if we require low power. Supercapacitors can complement battery-power by allowing rapid charge and discharge cycles. Accordingly, supercapacitors complement batteries perfectly in the emerging energy-storage landscape and therefore the usage of a battery-supercapacitor hybrid structure is not only becoming increasingly common, but also inevitable.

In the light of the foregoing, we have attempted to develop a high-performance asymmetric supercapacitor (ASC) using one-dimensional (1-D) core-shell nanorods (NRs) employing low-cost, abundant and environment-friendly materials.⁴ Core-shell NRs for positive and negative electrodes are grown directly on highly conductive flexible stainless steel (SS) substrate precluding the use of any binder.⁵ Indeed, the use of 1-D nanostructures in place of bulk samples provides vast interacting sites between electrodes and the electrolyte.^{6,7} In a core-shell nanostructure, nanometer-thin shell layer of electroactive materials significantly shortens ion-diffusion path-length for effective ion-intercalation and deintercalation in conjunction with fast electron transfer to the core, while the highly conducting core, which serves as scaffold for electroactive shell, rapidly transfers the electrons to the current collector.^{7,8}

Hematite (α -Fe₂O₃) is a promising negative electrode material for electrochemical capacitors (ECs) due to its high electrochem-

ical activity, high theoretical-specific-capacitance, suitable negative-potential-window because of high hydrogen over-potential in aqueous electrolytes, mostly environment friendly and abundance in nature.^{8–11} However, poor electrical conductivity (\sim 10⁻¹⁴ S/cm) and short ion-diffusion length limit its electrochemical performance significantly that can be overcome by creating oxygen vacancies within α -Fe₂O₃ thin films.^{9,11,12} Likewise, zinc oxide (ZnO) is an attractive material for solar cells owing to its higher electron mobility as compared to TiO₂.¹³ ZnO also has the advantages of low cost, easy fabrication, environment friendliness and most importantly higher electronic conductivity (10⁻³ to 1 S/cm) as compared to α -Fe₂O₃.^{14,15} Graphitic-carbon is an ubiquitously used electroactive material for batteries and capacitors due to its high electrostatic and mechanical strength.^{3,16,17}

In this communication, we report studies on an ASC using ZnO/ α -Fe₂O₃ and ZnO/C core-shell NRs as its respective negative and positive electrode materials. Interestingly, both positive and negative core-shell electrodes show compelling improvement in capacitance values in relation to their component materials and, as a consequence, the fabricated ZnO/ α -Fe₂O₃//ZnO/C core-shell NR ASC cell exhibits an energy density of \sim 41 Wh/kg and a power density as high as 7 kW/kg within the operating potential window of 0 to 1.8 V in an aqueous electrolyte.

Experimental

Preparation of ZnO NR arrays on SS substrate as the core material.—Well aligned ZnO NRs were grown on SS substrate by a modified seed-assisted hydrothermal synthesis procedure reported elsewhere.¹⁸ As the first step, ZnO nanocrystal seeds were prepared by reducing zinc acetate dihydrate (0.01 M) with sodium hydroxide (0.03 M) in ethanol solution at 60°C with continuous stirring for 2 h. The resultant nanocrystals were uniformly dispersed in the solution. Subsequently, the nanocrystals were drop-casted on properly cleaned and polished SS substrates for several times followed by drying at 150°C for 15 min to increase particle adhesion on substrate surface. After uniformly coating with seed layer, the substrates were placed horizontally inside a teflon-lined stainless steel autoclave containing zinc nitrate dihydrate (0.025 M) and hexamethylenetetramine (0.025 M) followed by heating at 90°C for 6 h for the growth of ZnO NR

*Electrochemical Society Member.

**Electrochemical Society Fellow.

^zE-mail: akshukla2006@gmail.com; sarma@sscu.iisc.ernet.in; deb.sarkar1985@gmail.com

arrays. The substrates with white ZnO layer were taken out from the autoclave, copiously washed with distilled water and ethanol and dried in an air oven at 60°C overnight. Finally, ZnO NRs were annealed in a tube furnace in H₂ atmosphere at 350°C for 3 h.

Preparation of ZnO/ α -Fe₂O₃ core-shell NRs as the negative electrode material.—ZnO/ α -Fe₂O₃ core-shell NR arrays were prepared by depositing α -Fe₂O₃ on ZnO NRs by spin-coating method. For this purpose, ethanol solution of ferric chloride hexahydrate (0.05 M) was drop casted onto ZnO NR arrays and spin dried at 3000 rpm for 30 s. The dried samples were subsequently heated at 250°C for 5 min to improve particle adhesion at NR surface. White-colored substrate turned yellow indicating the formation of FeOOH on repeating the procedure 7 times. The as prepared core-shell NRs were annealed in N₂ atmosphere at 400°C for 1 h to completely convert FeOOH to α -Fe₂O₃ with change in substrate color from yellow to brick red. α -Fe₂O₃ nanoparticles were also grown directly on SS substrate under identical conditions.

Preparation of ZnO/C core-shell NRs as the positive electrode material.—To prepare ZnO/C core-shell NR arrays, ZnO-deposited SS substrate was immersed into 50 ml of 0.5 M glucose aqueous solution for 24 h for adequate adsorption of glucose molecules onto NR surface. Subsequently, the SS foil was taken out and dried at 60°C followed by annealing in Ar atmosphere at 500°C for 5 h to allow complete carbonization of glucose shell onto ZnO NRs. For comparison, C shells were also grown directly on SS substrate under similar conditions.

Assembling the asymmetric supercapacitor cell.—The prototype ASC cell was fabricated by separating ZnO/ α -Fe₂O₃ and ZnO/C core-shell NR electrodes each of 1 × 1 cm² in size, with a polypropylene-mesh separator followed by encapsulation with polyethylene-terephthalate (PET) films to prevent electrolyte leakage.

Materials characterization and electrochemical measurement techniques.—Morphology, structure and composition of different electrode materials were investigated using field emission SEM (FE-SEM, FEI, Quanta FEG 650), TEM (TEM, FEI TECNAI G2 TF20ST), XRD (XRD, PANalytical Empyrean X-ray Diffractometer) and Raman spectroscopy (WITec, Nd:YAG laser with $\lambda = 532$ nm). X-ray-absorption (XAS) structure at the Fe *L*-edge and Zn *L*-edge were obtained at I-1011 beam line at the Max II storage ring, in the MAXLAB Synchrotron Radiation Laboratory, Sweden, and were recorded in surface sensitive total-electron-yield (TEY) mode. Loading density of the electroactive materials was calculated using a microbalance by measuring the mass difference before and after the deposition.

Electrochemical characterizations for as prepared samples were carried out on a software-controlled conventional three-electrode electrochemical work station (AutoLab PGSTAT 302N) comprising as prepared samples as working electrode, a Pt foil as counter electrode along with a Saturated Calomel Electrode (SCE, Hg/Hg₂Cl₂) as reference electrode in 0.5 M aqueous Na₂SO₄ solution. Electrochemical impedance spectroscopy (EIS) on the samples was performed in the same electrochemical cell in the frequency range between 10 mHz and 1 MHz with an operating ac field amplitude of 5 mV.

Results and Discussion

Morphology and elemental analyses.—Seed-mediated hydrothermal synthesis yields arrays of ZnO NRs on a large scale on polished SS substrate. Scanning electron microscopy reveals uniform coverage of ZnO NR arrays on substrate with diameters of ~100–150 nm and lengths of ~3–4 μ m (Fig. 1a). As also observed, NRs are hexagonal in shape due to hexagonal Wurtzite crystal structure of ZnO with smooth surface and sharp tip because of nucleation and growth procedures, as shown in Fig. 1b. However, surface morphology of NRs changed significantly and became very rough after deposition of α -Fe₂O₃ nanoparticles on ZnO NR surface, as can be seen in Fig. 1c

and inset to Fig. 1c, without any change in NR structure and alignment. TEM analysis further confirms uneven surface morphology of ZnO/ α -Fe₂O₃ core-shell NR (Fig. 1d and Fig. S1a (supplementary material)) and thickness of α -Fe₂O₃ shell is found to vary between 4 nm and 8 nm. HRTEM image reveals aligned lattice fringes of ZnO core oriented along [0001] direction with lattice spacing of 0.26 nm that corresponds to (002) crystal planes of ZnO.^{13,19} Core-shell structure and chemical composition of the nanorod arrays is confirmed through the energy filtered TEM images, as shown in Figs. 1e–1g. EDS elemental mapping clearly suggests higher concentration of Zn at the core of the nanorod, whereas, Fe mainly resides at the edges forming cylindrical shell layer in the core-shell structure. Fig. 1h displays SEM image for carbon-coated ZnO NRs exhibiting nearly smooth covering of carbon shell onto NR surface. TEM images, as shown in Fig. 1i and Fig. S1b (supplementary material), further confirm uniform and continuous coating of amorphous carbon shell layer on ZnO NRs with an average thickness of 6 nm.

Crystal structure of the as-synthesized ZnO/ α -Fe₂O₃ core-shell nanorods is investigated through XRD analysis and the corresponding XRD pattern (Fig. S2, supplementary material) comprises peaks that can be well indexed with different characteristic peaks of Wurtzite ZnO (JCPDS # 36–1451),^{19,20} rhombohedral α -Fe₂O₃ (JCPDS #89–0597)²⁰ and the SS substrate. However, weak signal in the diffraction pattern further suggests the formation of very thin layer of α -Fe₂O₃ over ZnO. To further elucidate the change in local environment and oxidation states of individual elements present in these composite electrode materials (with respect to the constituent ZnO and α -Fe₂O₃) as well as for studying the feature of the conduction band, room temperature X-ray absorption spectroscopy measurements are carried out as a sensitive local structure probe. Fig. 2a shows X-ray absorption spectra (XAS) for Zn *L*-edge where the spectral feature A corresponds to Zn 4*s* derived state and has been proposed to be associated to the σ -type interaction between Zn and O planes, while the features from B–D are associated with the Zn 4*d* derived states.²¹ This *L*-edge spectrum agrees well to the electron energy loss spectroscopy reports and also with XAS spectrum obtained for ZnO nanorods and ZnO thin films reported elsewhere.^{21–23} However, it is important to note here that the intensity of feature A in the present ZnO nanorod electrode materials is significantly less as compared to the same reported for pure ZnO powder.²⁴ This can be attributed to the intrinsic defects, mainly oxygen vacancies present in the system that result in partially occupied 4*s* state. Interestingly, the Zn *L*-edge XAS spectrum collected from the ZnO/ α -Fe₂O₃ core-shell nanostructure as shown by the red-colored line in Fig. 2a shows a significant increase in the relative intensity of the spectral feature A as compared to other features. This significant relative increase suggests considerably reduced occupancy of Zn 4*s* derived states leading to an enhancement in the occupied Zn 2*p* to unoccupied Zn 4*s* transition. This further suggests that the formation of the ZnO/ α -Fe₂O₃ core-shell nanostructure is followed by a charge transfer out of Zn 4*s* states that were previously occupied due to the presence of oxygen vacancies, as described in the case of ZnO nanorods above.

The charge transfer from Zn 4*s* like states is further supported by Fe *L*_{2,3} XAS spectra, as shown in Fig. 2b, where the intensity of peaks reflects electron transfer from Fe 2*p* state to unoccupied Fe 3*d* orbital, namely Fe 2*p*_{3/2}–3*d* for *L*₃ (~708 eV photon energy) and Fe 2*p*_{1/2}–3*d* for *L*₂ edges (~722 eV photon energy).^{25,26} In the Fe *L*₃ edge, we can observe a strong peak at higher binding energy (~709.5 eV) followed by a shoulder at lower binding energy side (~707.8 eV). It is well known from the literature that Fe³⁺ species in an oxide octahedral crystal-field environment exhibit a prominent feature at higher binding energy followed by a relatively weak shoulder at lower energy, while an Fe²⁺ species in the same environment produce the main feature at lower photon energy followed by a very small and relatively broad shoulder at higher binding energy.²⁷ Such strong contrast in both spectra provide an easy qualitative way of determining the average 3*d* occupancy in Fe atom. For α -Fe₂O₃ electrode, the spectral shape clearly indicates that it is Fe³⁺ rich. However, in the ZnO/ α -Fe₂O₃ core-shell nanostructure, the relative intensity of the left hand side shoulder has increased which qualitatively indicates the

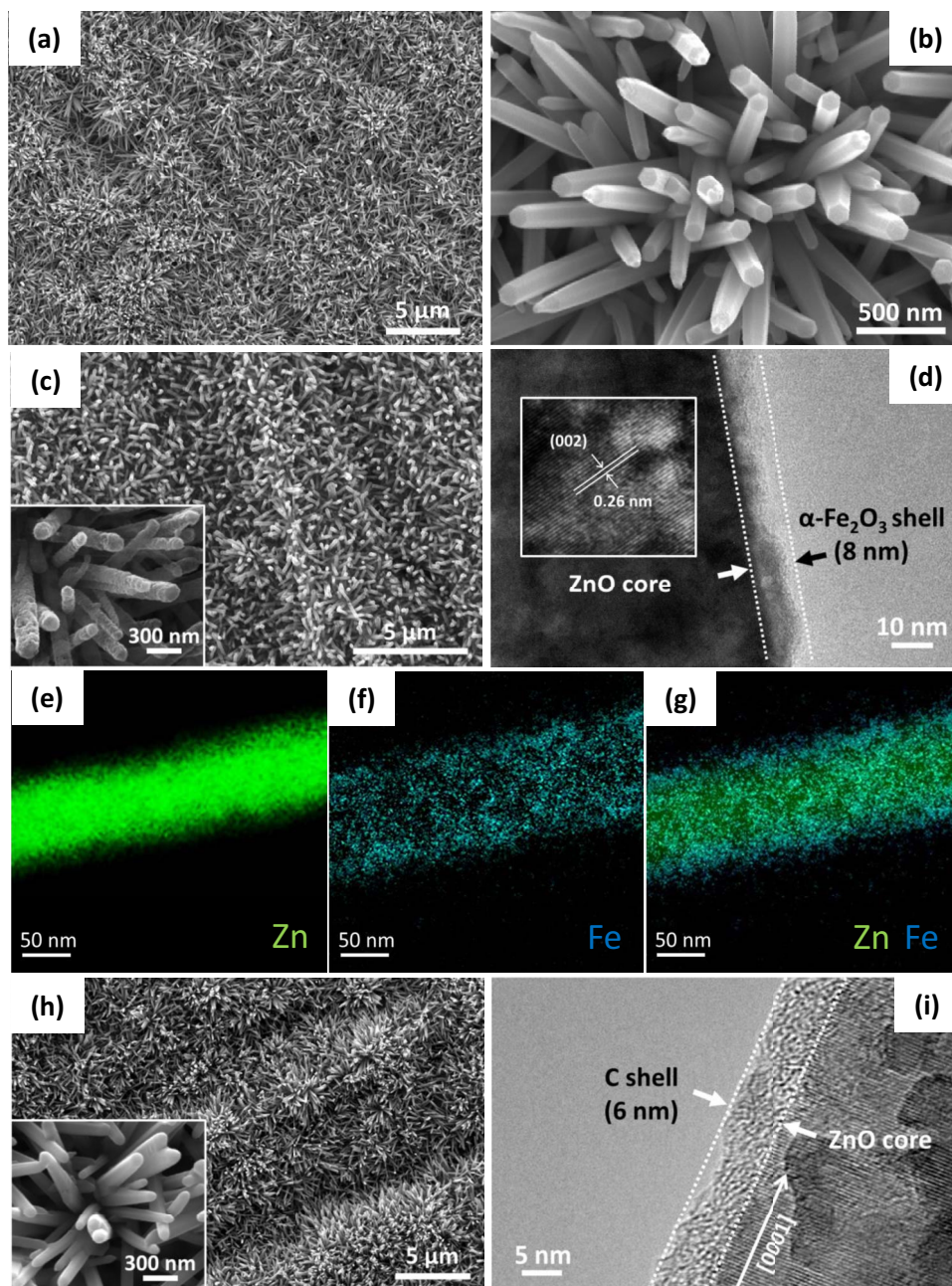


Figure 1. (a) FESEM image of high density ZnO NRs grown on SS substrate; (b) shows hexagonal shape and smooth surface morphology of individual ZnO NRs; (c) FESEM image of ZnO/ α -Fe₂O₃ core-shell NRs grown on SS substrate, inset image shows rough surface morphology after α -Fe₂O₃ coating; (d) TEM image for ZnO/ α -Fe₂O₃ core-shell NR, inset shows high resolution TEM image; (e)-(g) depict energy-filtered TEM (EFTEM) images, reflecting mapping of different metallic elements present in ZnO/ α -Fe₂O₃ core-shell NR; (h) depicts high-density ZnO/C core-shell NRs grown on SS substrate; TEM image for one such core-shell NR is shown in (i).

Fe³⁺ reduction. Therefore, both Fe *L*-edge and Zn *L*-edge XAS spectra concurrently suggest that some electron transfer from the Zn 4*s* like states to Fe 3*d* level via oxygen is taking place upon the formation of the heterojunction interface.

Crystallization of ZnO and successful deposition of a carbon shell on ZnO NR surface are further confirmed through Raman spectroscopy and corresponding Raman spectra for as synthesized ZnO and ZnO/C core-shell NRs are depicted in Fig. 2c. In ZnO Raman spectrum, peak at ~ 438 cm⁻¹ can be assigned to a nonpolar E₂ (high) optical phonon mode that corresponds to the band characteristics of wurtzite hexagonal phase of ZnO.^{28,29} The peak at ~ 380 cm⁻¹ is due to the A₁ (TO) mode, whereas, peaks around 202 and 330 cm⁻¹ are due to resonance conditions and can be assigned to acoustic phonon overtone

and optical phonon overtone modes with A₁ symmetry, respectively.³⁰ Moreover, the broad peak around 1145 cm⁻¹ belongs to the Raman 2LO mode.³¹ Raman spectra for ZnO/C core-shell NRs is characterized by two prominent peaks at ~ 1360 cm⁻¹ and ~ 1590 cm⁻¹ which correspond to the D and G bands, respectively, characteristic of graphitic carbon with sp² hybridization, with additional peaks at ~ 330 , 380 and 438 cm⁻¹ characteristic of wurtzite ZnO.^{17,31} The presence of intense D and G bands is itself an evidence of successful coating of amorphous graphitic carbon layer on ZnO NR surface.

Electrochemical characterization of negative and positive electrodes.—Electrochemical characterization of the electrodes comprising ZnO/ α -Fe₂O₃ and ZnO/C core-shell NRs are performed in

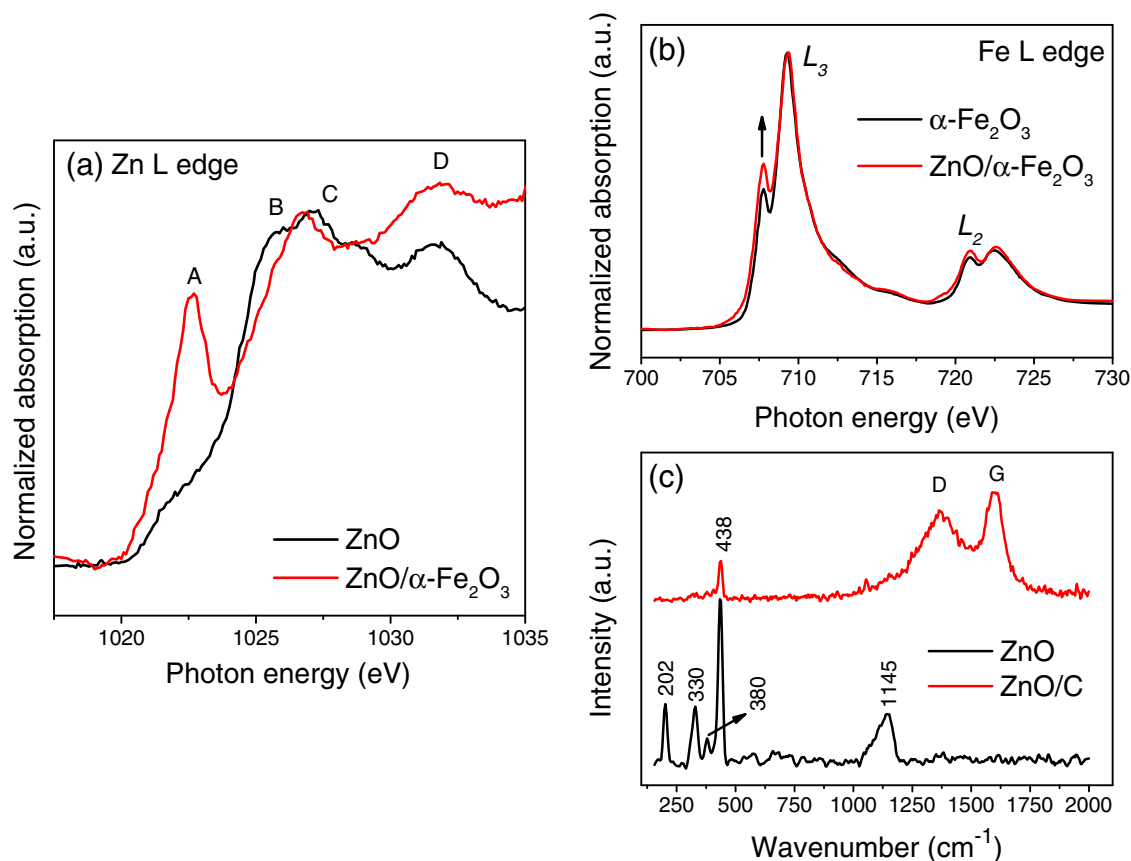


Figure 2. (a) Zn *L*-edge XAS spectra for pristine ZnO NRs and ZnO/ α -Fe₂O₃ core-shell NRs, (b) comparison of Fe *L*-edge XAS spectra recorded from standard α -Fe₂O₃ and ZnO/ α -Fe₂O₃ core-shell NR, and (c) Raman spectra of pristine ZnO NRs and ZnO/C core-shell NR arrays.

0.5 M aqueous Na₂SO₄ solution with Pt foil as the counter electrode with respect to SCE. Fig. 3a compares the cyclic voltammograms (CVs) obtained for ZnO NRs, ZnO/ α -Fe₂O₃ core-shell NRs along with α -Fe₂O₃ thin film grown directly on SS substrate at a scan rate of 100 mV/s within the potential window between 0 V and -0.85 V vs SCE. As can be seen from the data, current density for α -Fe₂O₃ thin film is significantly higher than ZnO owing to higher electrochemical activity of the former. Interestingly, electrochemical performance of ZnO/ α -Fe₂O₃ core-shell NRs is found to be significantly higher as compared to both of its individual components, namely ZnO and α -Fe₂O₃. Such an improvement can be attributed to increased electrochemical surface area due to NR designing of electroactive materials along with easy charge transportation across thin α -Fe₂O₃ shell to highly conductive SS substrate through ZnO core due to band engineering. In the light of the fact that ZnO has high electronic conductivity due to its intrinsic oxygen vacancies and lower work function as well as lower electron affinity compared to α -Fe₂O₃, which cause a band bending toward ZnO during formation of ZnO/ α -Fe₂O₃ *n/n* heterojunction, further facilitates electron transfer from α -Fe₂O₃ shell to ZnO core during redox reactions.^{20,32} Furthermore, annealing of FeOOH in N₂ atmosphere during conversion to α -Fe₂O₃ significantly enhances the shell electron density through incorporation of excessive amounts of oxygen vacancies in α -Fe₂O₃ lattice, thus improving its electronic conductivity as well. Furthermore, thin porous layer of α -Fe₂O₃ shortens ion-diffusion length for fast-ion motion and charge transfer. Such intrinsic properties of ZnO and α -Fe₂O₃ act synergistically to explain enhanced electrochemical performance of ZnO/ α -Fe₂O₃ core-shell nanostructure over its component materials. We have also recorded cyclic voltammograms for α -Fe₂O₃ thin film and ZnO/ α -Fe₂O₃ core-shell NR electrodes at varying scan rates between 10 mV/s and 400 mV/s within the potential window of 0 to

-0.85 V vs SCE, as shown in Fig. S3 (supplementary material). All the CV curves exhibit semi-rectangular shape, which is indicative of pseudocapacitive behavior of α -Fe₂O₃, and might be due to the Fe³⁺/Fe²⁺ reversible redox couple in aqueous electrolyte. However, as the electrochemical response of ZnO is negligible as compared to α -Fe₂O₃ based electrodes, specific capacitance of all electrodes is calculated by considering the mass of deposited α -Fe₂O₃ only, which is found to be ranging between 35 to 40 μ g/cm² in these electrodes; their variation with scan rate is depicted in Fig. 3b. Interestingly, ZnO/ α -Fe₂O₃ core-shell NR electrode exhibits a maximum specific capacitance of 491.7 F/g at a scan rate of 10 mV/s, which is significantly higher than α -Fe₂O₃ thin film electrode that exhibits only 295 F/g at the same scan rate. Furthermore, ZnO/ α -Fe₂O₃ core-shell NRs electrode retains 65.7% of its capacitance when the scan rate is increased from 10 mV/s to 400 mV/s while α -Fe₂O₃ thin film electrode could retain only 50.3% of initial capacitance during a similar increase in scan rate. Such a high capacitance and high-rate capability of the core-shell NR electrode can be attributed to its higher effective surface area for surface-based faradaic reactions, higher electronic conductivity of individual electrode materials and lower charge-transfer-resistance due to band bending. Additionally, pores on the core/shell NR surface can effectively serve as hydroxyl ion reservoir even at higher scan rates that also enhances the rate capability. However, a decrease in capacitance with increasing scan rate is primarily due to limited availability of electro-active surface at higher scan rates which is contrary to the case with lower scan rates where almost all possible surfaces and pores could be accessible for faradaic reactions. Furthermore, a comparison of galvanostatic charge/discharge data in Fig. S4 (supplementary material) shows smallest *IR*-drop along with significantly enhanced charge/discharge profile for ZnO/ α -Fe₂O₃ core-shell NRs electrode as compared to α -Fe₂O₃ thin film and ZnO NR electrodes, which again

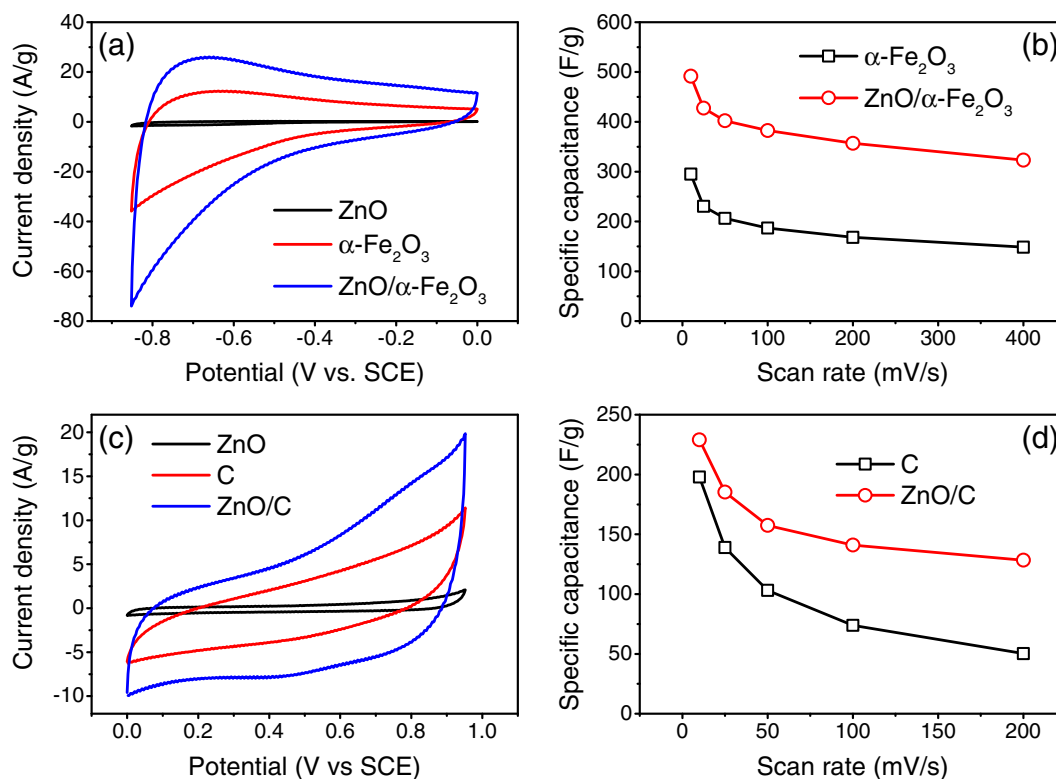


Figure 3. (a) Cyclic voltammograms recorded for ZnO, $\alpha\text{-Fe}_2\text{O}_3$ and ZnO/ $\alpha\text{-Fe}_2\text{O}_3$ core-shell NRs electrodes at the scan rate of 100 mV/s; (b) comparison of specific capacitances of $\alpha\text{-Fe}_2\text{O}_3$ and ZnO/ $\alpha\text{-Fe}_2\text{O}_3$ core-shell NRs electrodes, calculated from CV curves, as a function of scan rate; (c) comparison of cyclic voltammograms collected for ZnO, C and ZnO/C core-shell NRs electrodes at a scan rate of 100 mV/s and (d) variation of specific capacitances for C and ZnO/C core-shell NR electrodes as a function of scan rate.

signifies higher electronic conductivity and improved electrochemical performance for the nano-heterojunction electrode.

Electrochemical characterization of ZnO/C core-shell NR electrode within the potential window between 0 V and 0.95 V vs SCE is also performed keeping other measurement conditions akin to that for iron-oxide-based samples. The data are compared with those obtained for pristine ZnO NR electrode along with an amorphous-carbon-thin-film electrode directly grown on SS substrate, where the loading density for C is comparable (20–30 $\mu\text{g}/\text{cm}^2$). As depicted in Fig. 3c, current density increases significantly after carbon coating on ZnO NRs. The density is also higher than the carbon thin film electrode, reflecting improved electrochemical performance for ZnO/C core-shell NR electrode. However, as calculated from the cyclic voltammograms obtained at varying scan rates between 10 mV/s and 200 mV/s within the potential window of 0 to 0.95 V vs. SCE (as shown in Fig. S5, supplementary material), ZnO/C core-shell NR electrode exhibits a specific capacitance of 229 F/g, considering the mass of deposited C only, at a scan rate of 10 mV/s, while carbon thin film electrode exhibits 198 F/g at the same scan rate (Fig. 3d). More interestingly, as the scan rate increases from 10 mV/s to 200 mV/s, ZnO/C core-shell NR electrode exhibits a capacitance retention of 56% which is more than twice of that observed for carbon-thin-film-based electrode, which has only 25% retention at 200 mV/s. Such an increase in capacitance and improved rate capability for ZnO/C core-shell NR electrode can be attributed to the increased active surface area for double-layer formation over the carbon surface in conjunction with higher electronic conductivity of carbon shell and ZnO core that ensures good electrical contact of ZnO/C core-shell NRs with the substrate, thus facilitating charge transfer even at higher scan rates. Furthermore, as carbon has enough mechanical strength, it can sustain strain caused by the volume variation of ZnO core that prevents its disintegration during repeated ion-intercalation/deintercalation processes.^{16,17}

Electrochemical characterization of assembled ASC.—From single electrode measurements, it is seen that ZnO/C core-shell NR electrode exhibits stable electrochemical behavior within the potential window of 0 to 0.95 V against SCE, whereas a stable potential window of 0 to -0.85 V against SCE is established for ZnO/ $\alpha\text{-Fe}_2\text{O}_3$ electrode with core-shell NRs. Accordingly, by adding the voltage windows, one can expect that the asymmetric cell comprising ZnO/C core-shell NRs as positive electrode and ZnO/ $\alpha\text{-Fe}_2\text{O}_3$ core-shell NRs as negative electrode should give an operational cell-voltage of 1.8 V. Fig. 4a and Fig. S6 (supplementary material) depict cyclic voltammetry data and charge/discharge curves, respectively, obtained for the ZnO/ $\alpha\text{-Fe}_2\text{O}_3$ //ZnO/C asymmetric supercapacitor (ASC) prototype cell with core-shell NRs at different potential windows, in 0.5 M Na_2SO_4 aqueous electrolyte. As observed, there is a striking improvement in the electrochemical performance of ZnO/ $\alpha\text{-Fe}_2\text{O}_3$ //ZnO/C core-shell NRs ASC when the potential window is extended from 0.8 V to 1.8 V. Fig. 4b depicts the evolution of performance parameters with increasing cell potential where the specific capacitance is found to increase from 9.3 F/g to 37.1 F/g ($\sim 400\%$ increment) with increase in cell potential from 0.8 V to 1.8 V. More interestingly, the energy density (E) of the ASC, calculated using equation $E = 1/2 C_{sp} V^2$, where, C_{sp} being the specific capacitance and V is the potential window, increases from 0.83 Wh/kg to 16.7 Wh/kg, which accounts to $\sim 2000\%$ improvement with increase in cell potential. Therefore, a stable potential window of 0 to 1.8 V has been chosen in the following electrochemical measurements for ZnO/ $\alpha\text{-Fe}_2\text{O}_3$ //ZnO/C core-shell NRs ASC.

All cyclic voltammograms obtained for the ASC at varying scan rates between 10 mV/s to 200 mV/s within specified potential window of 0 to 1.8 V are nearly rectangular as shown in Fig. S7 (supplementary material), which represents ideal capacitor like behavior with fast charge/discharge characteristics. Furthermore, a rapid change in current especially at cutoff potentials represents fast charge-transfer

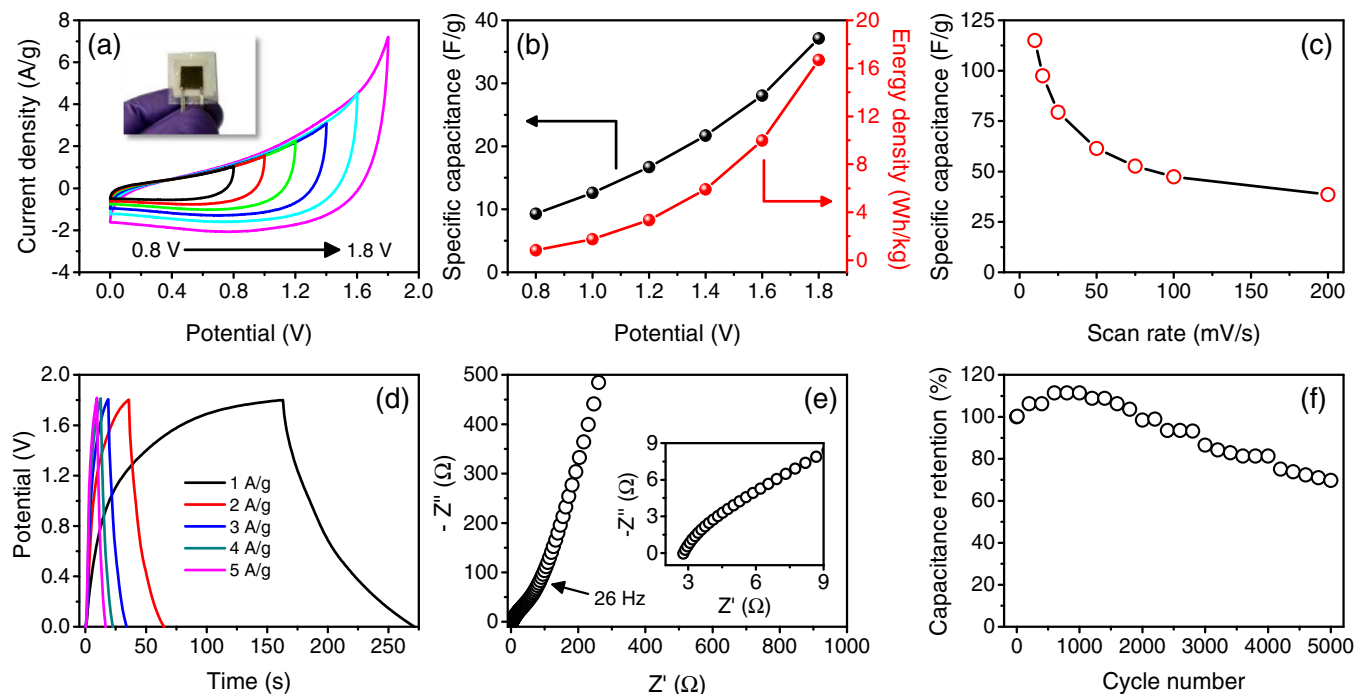


Figure 4. (a) Cyclic voltammograms of the ZnO/ α -Fe₂O₃//ZnO/C core-shell NR ASC cell recorded within different operational potential windows, inset shows digital image of the prototype cell having dimension of $1 \times 1 \text{ cm}^2$; (b) variation of specific capacitance and energy density calculated from CV curves as a function of operating potential window; (c) variation of specific capacitance as calculated from CV curves as function of potential scan rates; (d) Galvanostatic charge/discharge curves recorded at different current densities within a potential window of 1.8 V; (e) Nyquist plot ($-Z''$ vs Z' plot) for ASC cell within frequency range from 10 mHz to 1 MHz with an ac field amplitude of 5 mV, inset shows high frequency region of Nyquist plot and (f) cycling performance of ASC cell recorded at a scan rate of 100 mV/s during 5000 CV cycles.

during electrochemical processes owing to its small internal resistance. The specific capacitance values for the ASC calculated from CV data are plotted in Fig. 4c against scan rates. Maximum specific capacitance for the ASC is found to be $\sim 115 \text{ F/g}$ at a scan rate of 10 mV/s, which is significantly higher than other nanostructured iron oxide based ASCs reported recently, namely α -Fe₂O₃ NRs//MnO₂ ASC (23 F/g at scan rate of 10 mV/s),⁹ α -Fe₂O₃ nanoparticle//MnO₂ nanosheet ASC ($\sim 77 \text{ F/g}$ at scan rate of 10 mV/s),³³ MnFe₂O₄//AC ASC (51.9 F/g at scan rate of 5 mV/s),³⁴ multi-walled carbon nanotube- α -Fe₂O₃// multi-walled carbon nanotube (70 F/g at scan rate of 10 mV/s),³⁵ etc. The ASC reported in this study retains a capacitance value of $\sim 47 \text{ F/g}$ as the scan rate increases from 10 mV/s to 100 mV/s. Superior electrochemical performance for the ASC is further established by constant-current charge/discharge method and related data at different current-densities are shown in Fig. 4d and Fig. S8 (supplementary material). As can be seen from the data, discharge profile is almost symmetric to charging profile at lower discharge currents with very small ohmic drop (0.08 V at 0.5 A/g) implying smaller equivalent-series resistance for the ASC. However, at higher current-densities charge/discharge profiles become more symmetrical and linear, representing ideal-capacitive behavior with fast charge/discharge characteristics for the ASC. The increase in ohmic drop with increasing current densities can be ascribed to less accessible electrode surface at higher currents akin to that observed during increasing scan rates. From the discharge profile, maximum value of specific capacitance is found to be $\sim 92 \text{ F/g}$ at a discharge current density of 0.5 A/g, which is also significantly higher than the values reported for other iron-oxide-based ASCs, like MnO₂//FeOOH ASC (51 F/g at load current of 0.5 A/g),³⁶ Fe₃O₄//MnO₂ ASC (23 F/g at load current of 0.27 A/g),³⁷ LiMn₂O₄ // MnFe₂O₄ ASC ($\sim 50 \text{ F/g}$ at load current of 0.5 A/g),³⁸ etc., and is also better than some carbon-based ASCs such as graphene hydrogel//MnO₂ ASC (41.7 F/g at load current of 1 A/g),³⁹ activated carbon//MnO₂ ASC (31 F/g at load current of

0.55 A/g)⁴⁰ and activated carbon//NiO ASC (73.4 F/g at load current of 0.1 A/g).⁴¹

To estimate the internal resistance and response time for the ASC, we have carried out electrochemical impedance spectroscopy (EIS) and corresponding Nyquist plot ($-Z''$ vs Z' plot) is shown in Fig. 4e. At higher frequencies, intercept of Nyquist curve with real axis yields equivalent-series resistance (ESR) which is found to be $\sim 2.8 \Omega$ in this case, implying good electrical conductivity for the electrolyte and a low internal-resistance for the electrode. Low frequency region of the Nyquist curve is more inclined toward imaginary axis signifying ideal capacitive behavior of the cell. However, the “knee frequency”, which defines the crossover between purely resistive and capacitive behaviors while moving from high frequency to low frequency region, is found to be $\sim 26 \text{ Hz}$ for the ASC, implying that ideal capacitive behavior with almost all available charge can only be attained below this frequency. Furthermore, capacitive response frequency (f_0) calculated from the Bode plot shown in Fig. S9 (supplementary material) at a phase angle of -45° is about 25.7 Hz, which gives a response time as small as $\sim 39 \text{ ms}$, again implying fast charge/discharge characteristics of the ASC cell.

Superior capacitive performance of the ZnO/ α -Fe₂O₃//ZnO/C core-shell NR ASC can be ascribed to several factors, namely (a) nanostructured core-shell design of individual electrodes that provides a huge platform for surface-based faradaic/non-faradaic reactions resulting in an improved capacitance, (b) thin layers of electro-active materials, namely α -Fe₂O₃ and carbon, effectively reduce ion diffusion path lengths so as to ease ion intercalation/deintercalation together with fast electron transfer toward current collector through highly-conductive ZnO core, and (c) direct growth of electro-active materials on SS substrate (current collector) that has significant effect on reducing internal resistance of the system in addition to providing good structural integrity and mechanical stability to the system. Additionally, the carbon shell on ZnO core not only enhances capacitive

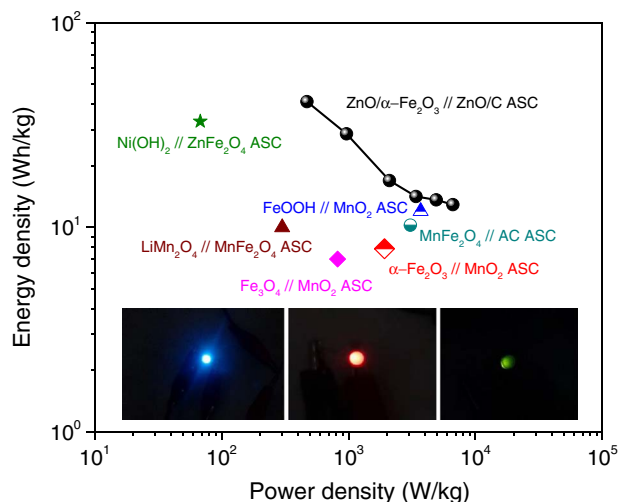


Figure 5. Ragone plot for ZnO/ α -Fe₂O₃//ZnO/C core-shell NR ASC cell; energy and power density values are also compared with the same for other reported ASC devices; inset images are the digital photographs of different LEDs powered by the assembled ASC cell.

performance through a double-layer formation but also acts as a structural buffer during electrochemical reactions, which is significant for the long-cycling stability of the system.

Fig. 4f reflects long-term cycling performance of assembled ZnO/ α -Fe₂O₃//ZnO/C core-shell NR ASC observed during CV analyses for 5000 cycles at a scan rate of 100 mV/s within the potential window of 0 to 1.8 V. Except the initial increase, which might be due to some activation processes, capacitance remains almost constant up to 2000 cycles with a capacitance retention of \sim 99%. The ASC cell can retain more than 81% of its initial capacitance after 4000 cycles, which decreases to \sim 70% after 5000 cycles. In aqueous electrolytes, the decay in capacitance can be attributed to dissolution of electroactive materials in electrolyte during cycling together with excess volume expansion due to continuous ion-insertion/deinsertion processes.^{8,33} The long-term cyclability of the ASC is comparable and even superior to other iron oxides and Carbon Nanotube (CNT) based ASC devices reported in the literature, namely MnO₂//FeOOH ASC (85% after 2000 cycles),³⁶ MnO₂//Fe₂O₃ ASC (91% after 3000 cycles),³³ MnO₂ NW/graphene/graphene ASC (79% after 1000 cycles)⁴² and RuO₂ /graphene/graphene ASC (95% after 2000 cycles).⁴³

Ragone plot that represents energy and power performance of an electrochemical cell is shown in Fig. 5 for ZnO/ α -Fe₂O₃//ZnO/C core-shell NR ASC cell. We have also compared the energy and power values with the same for other reported iron-oxide-based aqueous and solid-state ASC devices. Maximum energy-density that has been achieved for the ASC is 41.2 Wh/kg at a load-current density of 0.5 A/g with a corresponding power density of 471 W/kg. The energy density is found to be 13 Wh/kg with a maximum power density of \sim 7 kW/kg when the load current-density is increased by 10 times, representing an excellent rate performance for the ASC. Such compelling values of energy and power densities for the ZnO/ α -Fe₂O₃//ZnO/C core-shell NR ASC cell with a cell voltage of 1.8 V are better than other reported ASCs having different iron oxide nanostructures as the electrode material, namely 7 Wh/kg and 820 W/kg for Fe₃O₄//MnO₂ ASC,³⁷ 12 Wh/kg and 3700 W/kg for FeOOH//MnO₂ ASC,³⁶ 7.86 Wh/kg and 1918.5 W/kg for α -Fe₂O₃ NRs//MnO₂-ASC,⁹ 10 Wh/kg and 300 W/kg for LiMn₂O₄ // MnFe₂O₄ ASC,³⁸ 10.25 Wh/kg and 3076 W/kg for MnFe₂O₄//AC ASC,³⁴ 33 Wh/kg and 68 W/kg for Ni(OH)₂ // ZnFe₂O₄ ASC,⁴⁴ 37.8 Wh/kg and 648 W/kg for ZnCo₂O₄//MnO₂// α -Fe₂O₃ ASC,⁴⁵ 32.5 Wh/kg and 1.6 kW/kg for MnO₂ nanowires// α -Fe₂O₃ nanotube ASC,⁴⁶ and also exhibits significantly higher power density as compared to α -Fe₂O₃ nanoparticle//MnO₂ nanosheet ASC.³³

In order to study the practical implications of the aforesaid ASC, a prototype ASC (1 \times 1 cm²) is realized to light a Light-Emitting-Diode (LED). It is shown that single ASC can light a red LED after charging at 3 A/g for 10 s while a tandem device fabricated by connecting two ASC units (each 1 \times 1 cm²) in series, which has an extended potential window, can light blue and green LEDs even after charging for 10 s. Accordingly, the ZnO/ α -Fe₂O₃//ZnO/C core-shell NR ASC with environment friendly, stable and economically viable materials has potential to find applications in futuristic ecofriendly electronic devices.

Conclusions

The study provides a proof-of-concept to develop high-performance supercapacitors using core-shell type nanostructured electrode materials. Use of α -Fe₂O₃, ZnO and C in engineering core-shell nanorod electrodes, ZnO/ α -Fe₂O₃ negative and ZnO/C positive electrodes, effectively improves overall cell performance through surface-based faradaic and non-faradaic reactions together with fast-electron/ion transfer kinetics. ASC operates within a potential window of 0 to 1.8 V and delivers a specific capacitance of \sim 115 F/g at a scan rate of 10 mV/s. Maximum energy and power density values that have been achieved with the ASC are \sim 41 Wh/kg and \sim 7 kW/kg, respectively. Furthermore, the ASC exhibits compelling cycling stability with more than 80% capacitance retention after 4000 cycles with response time of \sim 39 ms. It is hoped that the reported performance of the ASC comprising core-shell nanostructures with environment-friendly materials as electrodes will open-up a new direction in energy storage. The study further strengthens that core-shell-based supercapacitors with long cycle-life could become a commercial reality in future.

Acknowledgments

DS is grateful to the Department of Science and Technology (DST), Government of India, for an 'INSPIRE Faculty Award' (IFA 14-MS-32). Authors thank Professor K. K. Nanda for his help in recording Raman spectra. Support from the Swedish Research Council (2014-06019) is also acknowledged.

References

- J. Tollefson, *Nature*, **456** 436 (2008).
- J. R. Miller and P. Simon, *Science*, **321** (5889), 651 (2008).
- P. Simon and Y. Gogotsi, *Nat. Mat.*, **7** (11), 845 (2008).
- D. Sarkar, A. Shukla, and D. D. Sarma, Inaidn Pat. Application No. 201641020589 (2016).
- D. Sarkar, A. Shukla, and D. D. Sarma, *ACS Energy Lett.*, **1** (1), 82 (2016).
- M. J. Bierman and S. Jin, *Energy Environ. Sci.*, **2** (10), 1050 (2009).
- J. Yan, E. Khoo, A. Sumboja, and P. S. Lee, *ACS Nano*, **4** (7), 4247 (2010).
- D. Sarkar, G. G. Khan, A. K. Singh, and K. Mandal, *J. Phys. Chem. C*, **117** (30), 15523 (2013).
- X. Lu, Y. Zeng, M. Yu, T. Zhai, C. Liang, S. Xie, M.-S. Balogun, and Y. Tong, *Adv. Mater.*, **26** (19), 3148 (2014).
- Q. Qu, S. Yang, and X. Feng, *Adv. Mater.*, **23** (46), 5574 (2011).
- K. K. Lee, S. Deng, H. M. Fan, S. Mhaisalkar, H. R. Tan, E. S. Tok, K. P. Loh, W. S. Chin, and C. H. Sow, *Nanoscale*, **4** (9), 2958 (2012).
- Y. Lin, G. Yuan, S. Sheehan, S. Zhou, and D. Wang, *Energy Environ. Sci.*, **4** (12), 4862 (2011).
- S. H. Ko, D. Lee, H. W. Kang, K. H. Nam, J. Y. Yeo, S. J. Hong, C. P. Grigoropoulos, and H. J. Sung, *Nano Lett.*, **11** (2), 666 (2011).
- M. Law, L. E. Greene, J. C. Johnson, R. Saykally, and P. Yang, *Nat. Mat.*, **4** (6), 455 (2005).
- Y. Natsume, H. Sakata, T. Hirayama, and H. Yanagida, *J. Appl. Phys.*, **72** (9), 4203 (1992).
- G. Cui, Y.-S. Hu, L. Zhi, D. Wu, I. Lieberwirth, J. Maier, and K. Müllen, *Small*, **3** (12), 2066 (2007).
- J. Liu, Y. Li, R. Ding, J. Jiang, Yingying Hu, X. Ji, Q. Chi, Z. Zhu, and X. Huang, *J. Phys. Chem. C*, **113**, 5336 (2009).
- L. E. Greene, M. Law, J. Goldberger, F. Kim, J. C. Johnson, Y. Zhang, R. J. Saykally, and P. Yang, *Angew. Chem. Int. Ed.*, **42** (26), 3031 (2003).
- L. Xu, Q. Liao, J. Zhang, X. Ai, and D. Xu, *J. Phys. Chem. C*, **111** (12), 4549 (2007).
- D. Sarkar, G. G. Khan, A. K. Singh, and K. Mandal, *J. Phys. Chem. C*, **116** (44), 23540 (2012).

21. A. A. Mosquera, D. Horwat, A. Rashkovskiy, A. Kovalev, P. Miska, D. Wainstein, J. M. Albella, and J. L. Endrino, *Sci. Rep.*, **3**, 1714 (2013).
22. T. Mizoguchi, I. Tanaka, S. Yoshioka, M. Kunisu, T. Yamamoto, and W. Y. Ching, *Phys. Rev. B*, **70** (4), 045103 (2004).
23. J. W. Chiou, K. P. K. Kumar, J. C. Jan, H. M. Tsai, C. W. Bao, W. F. Pong, F. Z. Chien, M.-H. Tsai, I.-H. Hong, R. Klauser, J. F. Lee, J. J. Wu, and S. C. Liu, *Appl. Phys. Lett.*, **85** (15), 3220 (2004).
24. V. L. Pool, M. T. Klem, J. Holroyd, T. Harris, E. Arenholz, M. Young, T. Douglas, and Y. U. Idzerda, *J. Appl. Phys.*, **105** (7), 07B515 (2009).
25. S. Shen, J. Zhou, C.-L. Dong, Y. Hu, E. N. Tseng, P. Guo, L. Guo, and S. S. Mao, *Sci. Rep.*, **4** 6627 (2014).
26. L. Vayssieres, C. Sathe, S. M. Butorin, D. K. Shuh, J. Nordgren, and J. Guo, *Adv. Mater.*, **17** (19), 2320 (2005).
27. Y. Takahashi, V. K. Verma, G. Shibata, T. Harano, K. Ishigami, K. Yoshimatsu, T. Kadono, A. Fujimori, A. Tanaka, F. H. Chang, H. J. Lin, D. J. Huang, C. T. Chen, B. Pal, and D. D. Sarma, *Europhys. Lett.*, **108** (2), 27003 (2014).
28. M. Wang, F. Ren, J. Zhou, G. Cai, L. Cai, Y. Hu, D. Wang, Y. Liu, L. Guo, and S. Shen, *Sci. Rep.*, **5** 12925 (2015).
29. S. Zhang, B. Yin, H. Jiang, F. Qu, A. Umar, and X. Wu, *Dalton Trans.*, **44** (5), 2409 (2015).
30. M. Rajalakshmi, A. K. Arora, B. S. Bendre, and S. Mahamuni, *J. Appl. Phys.*, **87** (5), 2445 (2000).
31. Z. Yin, S. Wu, X. Zhou, X. Huang, Q. Zhang, F. Boey, and H. Zhang, *Small*, **6** (2), 307 (2010).
32. Z. Jun, L. Xianghong, W. Liwei, Y. Taili, G. Xianzhi, W. Shihua, W. Shurong, and Z. Shoumin, *Nanotechnology*, **22** (18), 185501 (2011).
33. G. S. Gund, D. P. Dubal, N. R. Chodankar, J. Y. Cho, P. Gomez-Romero, C. Park, and C. D. Lokhande, *Sci. Rep.*, **5** 12454 (2015).
34. K. V. Sankar and R. K. Selvan, *RSC Adv.*, **4** (34), 17555 (2014).
35. X. Zhao, C. Johnston, and P. S. Grant, *J. Mater. Chem.*, **19** (46), 8755 (2009).
36. W.-H. Jin, G.-T. Cao, and J.-Y. Sun, *J. Power Sources*, **175** (1), 686 (2008).
37. T. Brousse and D. Bélanger, *Electrochem. Solid-State Lett.*, **6** (11), A244 (2003).
38. Y.-P. Lin and N.-L. Wu, *J. Power Sources*, **196** (2), 851 (2011).
39. H. Gao, F. Xiao, C. B. Ching, and H. Duan, *ACS Appl. Mater. Interfaces*, **4** (5), 2801 (2012).
40. T. Cottineau, M. Toupin, T. Delahaye, T. Brousse, and D. Bélanger, *Appl. Phys. A*, **82** (4), 599 (2006).
41. C. Yuan, X. Zhang, Q. Wu, and B. Gao, *Solid State Ionics*, **177** (13–14), 1237 (2006).
42. Z.-S. Wu, W. Ren, D.-W. Wang, F. Li, B. Liu, and H.-M. Cheng, *ACS Nano*, **4** (10), 5835 (2010).
43. B. G. Choi, S.-J. Chang, H.-W. Kang, C. P. Park, H. J. Kim, W. H. Hong, S. Lee, and Y. S. Huh, *Nanoscale*, **4** (16), 4983 (2012).
44. A. Shanmugavani and R. K. Selvan, *RSC Adv.*, **4** (51), 27022 (2014).
45. W. Ma, H. Nan, Z. Gu, B. Geng, and X. Zhang, *J. Mater. Chem. A*, **3** (10), 5442 (2015).
46. P. Yang, Y. Ding, Z. Lin, Z. Chen, Y. Li, P. Qiang, M. Ebrahimi, W. Mai, C. P. Wong, and Z. L. Wang, *Nano Lett.*, **14** (2), 731 (2014).